

Light-matter interaction in a microcavity-controlled graphene transistor

Michael Engel^{1,2}, Mathias Steiner^{3,*}, Antonio Lombardo⁴, Andrea C. Ferrari⁴, Hilbert
v. Löhneysen^{2,5,6}, Phaedon Avouris³, and Ralph Krupke^{1,2,7,#}

¹*Institute of Nanotechnology, Karlsruhe Institute of Technology, 76021 Karlsruhe,
Germany*

²*DFG Center for Functional Nanostructures (CFN), 76031 Karlsruhe, Germany*

³*IBM Thomas J. Watson Research Center, Yorktown Heights, New York 10598, USA*

⁴*Engineering Department, University of Cambridge, Cambridge CB3 0FA, UK*

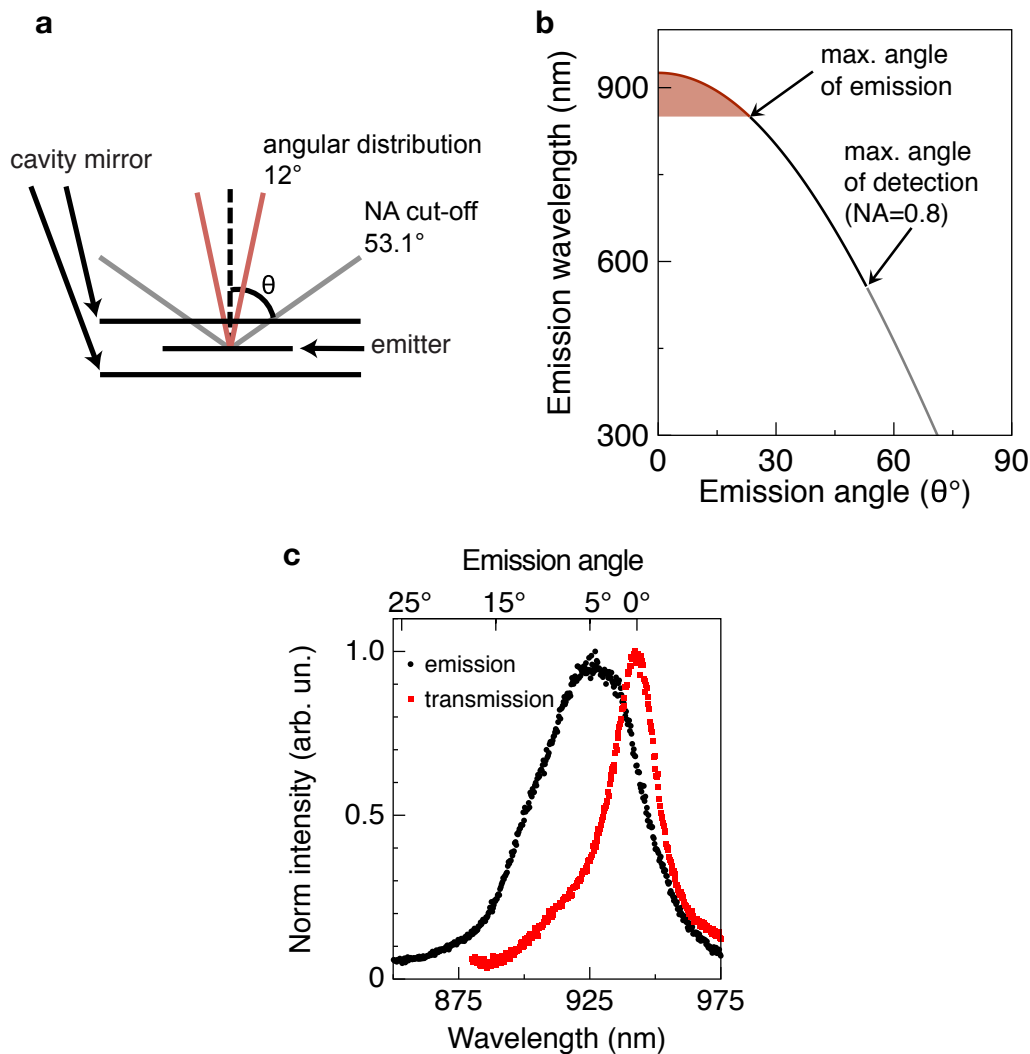
⁵*Physics Institute, Karlsruhe Institute of Technology, 76021 Karlsruhe, Germany*

⁶*Institute of Solid State Physics, Karlsruhe Institute of Technology, 76021 Karlsruhe,
Germany*

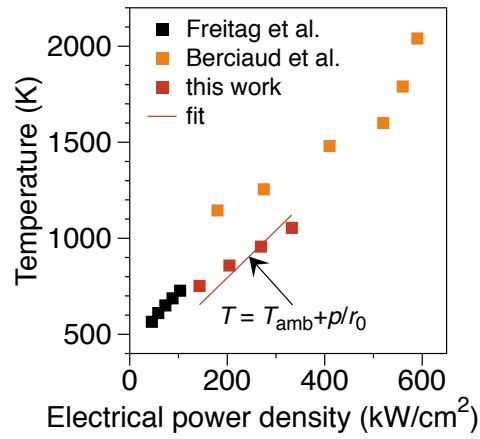
⁷*Department of Materials and Earth Sciences, Technische Universität Darmstadt,
64287 Darmstadt, Germany*

*[*msteine@us.ibm.com](mailto:msteine@us.ibm.com), [#krupke@kit.edu](mailto:krupke@kit.edu)*

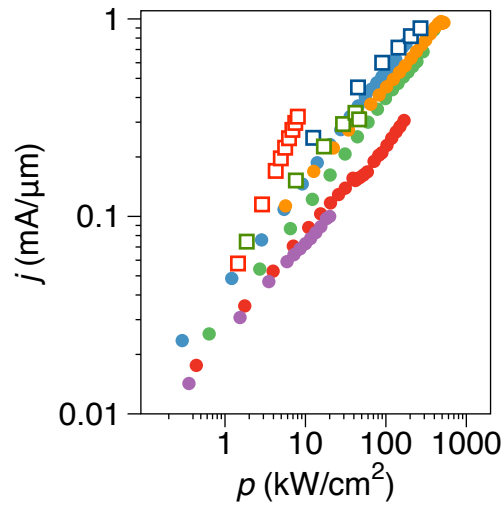
Supplementary Information



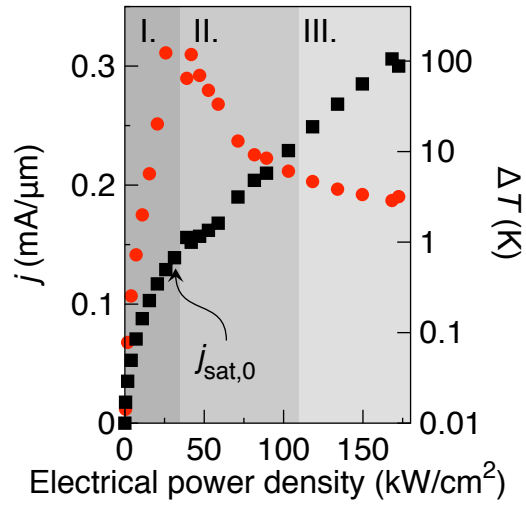
Supplementary Figure S1 | Angular distribution of microcavity-controlled thermal emission. a, Schematic showing the graphene layer placed between the two cavity mirrors. Also indicated are the maximum angle of detection and the angular distribution of the emitted light. **b,** Emission wavelength as a function of emission angle. No light emission can be observed for $\theta > 23^\circ$. **c,** On-axis transmission (red) and thermal emission (black) spectrum measured on the same device as a function of wavelength and emission angle, respectively. The maximum thermal emission intensity is observed at 5° while the collimated thermal emission lobe has an angular width of 12° (FWHM).



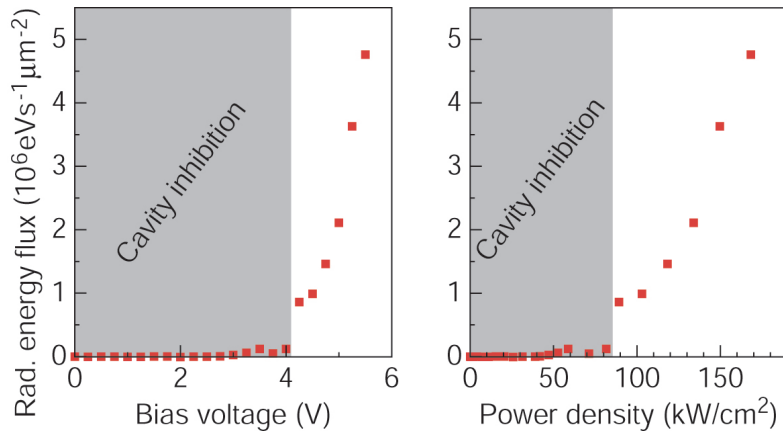
Supplementary Figure S2 | Temperature dependence of non-confined, free-space graphene transistors. Plotted is the temperature of graphene as function of injected electrical power density, in comparison with data taken from the literature^{11,12}. The temperature-values are extracted by fitting the measured, free-space thermal emission spectra of a reference graphene transistor (with the same dielectric layers and metal contacts, but without cavity mirrors) to a model of a two-dimensional black-body.



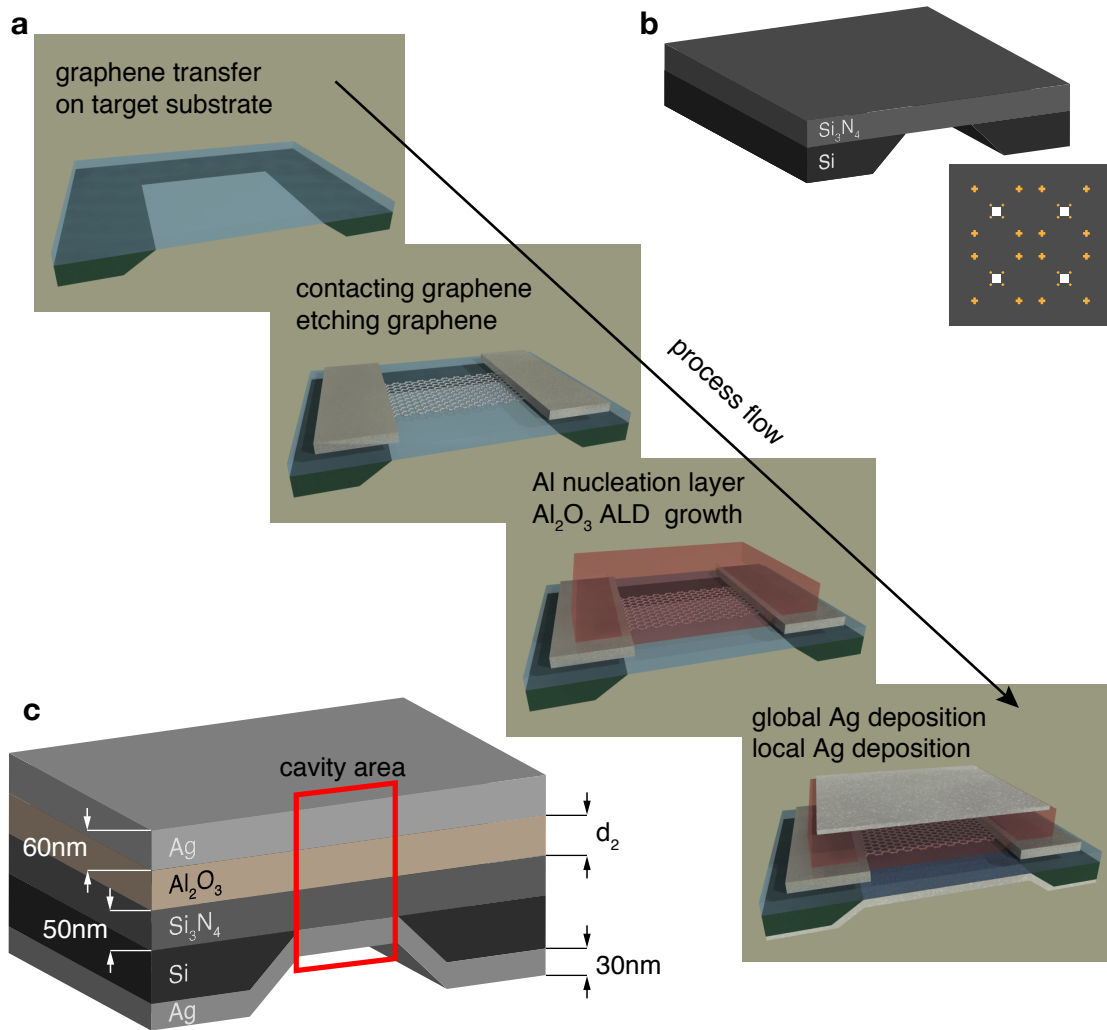
Supplementary Figure S3 | Comparison of electrical current levels in confined and non-confined graphene transistors. The experimental current density is plotted as function of electrical power density for a total of 8 graphene transistors. Microcavity-controlled graphene transistors (filled circles) consistently exhibit current saturation at lower electrical power densities than non-confined graphene transistors (open squares), along with a sudden increase of current density above threshold for thermal emission. Modifications of the electrical transport in microcavity-controlled graphene transistors that are in qualitative agreement with the data of the main text have been observed in a total of 5 devices.



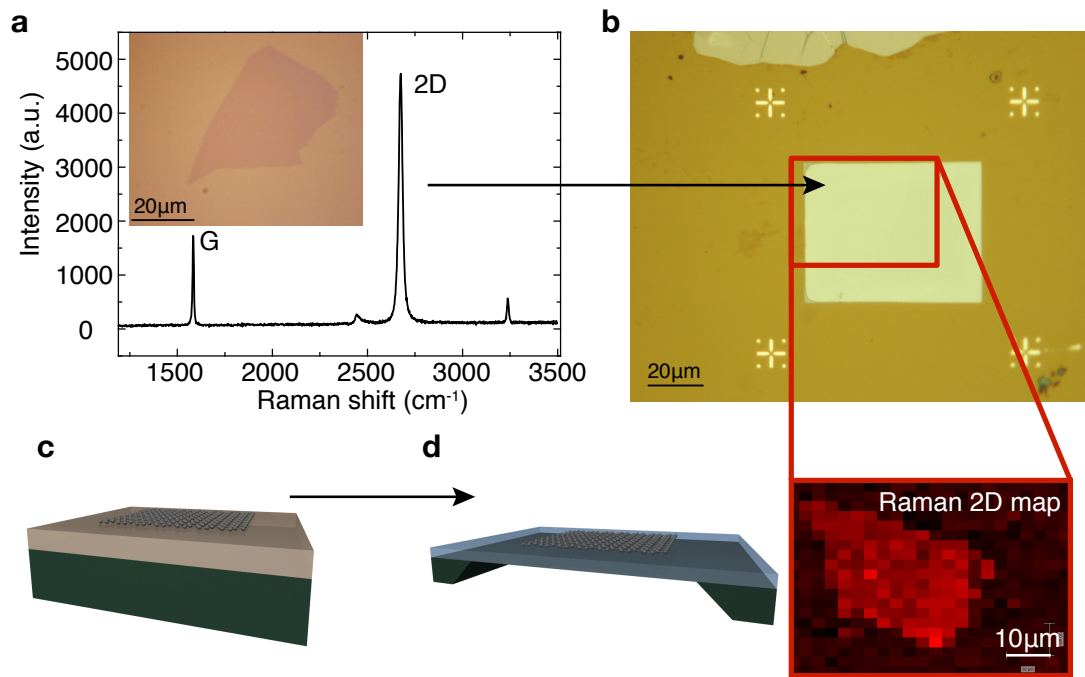
Supplementary Figure S4 | Temperature modifications of biased, cavity-confined graphene. Electrical current density (black squares) and relative temperature change (red circles) as function electrical power density. The cavity-confined graphene transistor heats up by ΔT as a consequence of the inhibition of thermal radiation (within regime I). Once thermal radiation sets in (threshold regime II.), the temperature elevation decreases.



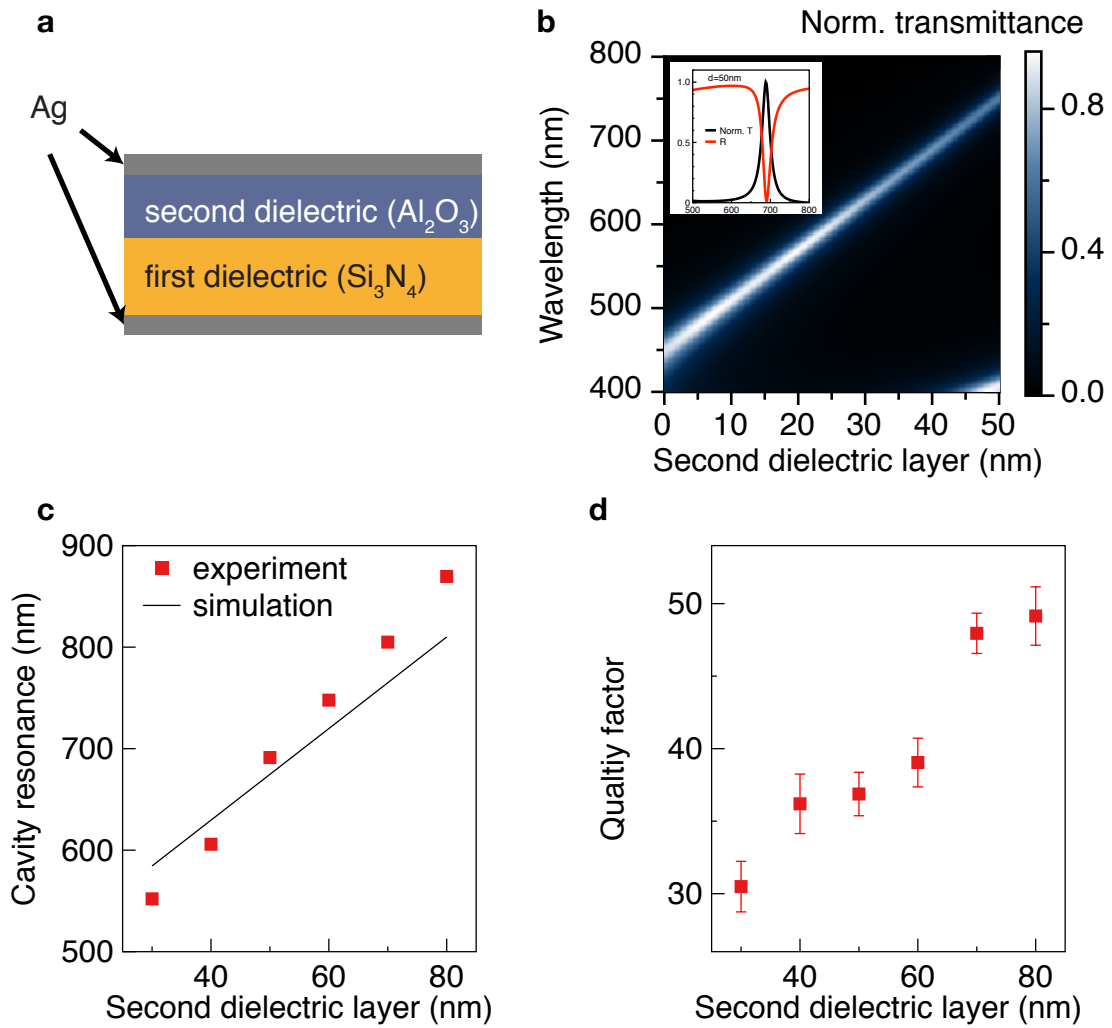
Supplementary Figure S5 | Radiated heat flow as function of bias voltage and electrical power density. Estimation at which rate heat is radiatively dissipated through cavity-controlled thermal light emission the measured light intensity is converted into an energy flux. By summing the measured photon flux in the spectral window of the cavity resonance and taking into account the detection conditions, we obtain the integrated energy flow that emanates from the device area of $1 \mu\text{m}^2$ at each bias point. Above threshold at 4V or 80kW/cm^2 , respectively, the device emits thermal photons having energy of 1.3eV ($\lambda \sim 925 \text{nm}$) which is equivalent to an overall heat transfer at a rate of $4.8 \times 10^6 \text{eV/s}$.



Supplementary Figure S6 | Design and process flow for integrating a graphene transistors and an optical microcavity. **a**, Process flow showing the main steps of monolithic integration. **b**, Schematic of the target substrate, a 50nm Si_3N_4 membrane with an area of $50 \times 50 \mu\text{m}^2$. Also shown is a top view schematic with the predefined metallic markers defined by e-beam lithography used for orientation during the transfer process and re-alignment for later lithography steps. **c**, Schematic of the multilayer stack with detailing the different materials and layer thickness. The red box highlights the microcavity.



Supplementary Figure S7 | Exfoliation and transfer of single layer graphene. **a**, Raman spectrum of an exfoliated, single-layer graphene flake. Inset: Optical microscope image of the exfoliated single layer graphene on Si/SiO₂. **b**, Optical microscope image of single-layer graphene after transfer on to 50nm Si₃N₄ membrane. Also shown is a spatial map of the 2D Raman intensity confirming the successful transfer. **c** and **d**, 3D visualizations of single layer graphene after exfoliation and transfer on to the target substrate.



Supplementary Figure S8 | Simulation and design of the optical microcavity. **a**, Schematic of the multilayer stack used for modeling the transmission/reflectance of the microcavity as a function of wavelength and dielectric layer thickness. **b**, False color plot of the normalized transmittance from the cavity shown in **a**. **c**, Cavity resonance wavelength obtained by measuring the reflectance from reference cavities with Al_2O_3 layer thickness between 30nm and 80nm. Each data point represents the average of 4 different cavities. The solid line is a result from the optical simulation shown in **b**. **d**, Cavity-quality factors of the reference samples shown in **c**. Each data point represents the average of 4 different cavities.

Supplementary Methods

Simulation and experimental verification of resonance wavelength and cavity-Q

The microcavity resonance is determined by the thickness of the Si₃N₄ and Al₂O₃ layers, i.e. the total thickness of the intra-cavity medium. In our case the Si₃N₄ layer thickness is fixed at 50nm while the thickness of the second intra-cavity medium Al₂O₃ can be freely adjusted. To determine the Al₂O₃ thickness to grow, we modeled the cavity resonance within a transfer matrix approach, i.e. a plane wave propagates through this multilayered cavity system and the electric field is evaluated at each boundary (see Supplementary Figure S7a). From the simulations we infer the proper Al₂O₃ thickness for a targeted cavity resonance wavelength (Supplementary Figure S7b). For validation of the simulations we build a series of reference cavities without graphene. The results in Supplementary Figure S7c demonstrate the level of control over the cavity resonance by adjusting the thickness of the alumina layer. The cavity-Q values achieved (see Supplementary Figure S7d) are in agreement with previous reports on planar cavities with metallic mirrors²⁸.

Microcavity-controlled thermal emission – angular distribution

We now analyze the angular distribution of the cavity-confined thermal light emission. According to reference 18, the following equation relates the emission wavelength λ to the emission angle θ with respect to the cavity normal (see Supplementary Figure S1),

$$\lambda = \frac{2Ln_{pol} \cos \theta}{(m - \Delta\phi/2\pi)}$$

where L is the geometrical mirror spacing (or cavity length), n_{pol} is refractive index of the intra-cavity medium, m is the mode order ($m=1$ in this case), and $\Delta\phi$ is the phase shift associated with light absorption in the metallic mirrors. The microscope objective used in our measurements has a numerical aperture of $NA=0.8$. This corresponds to a maximum detection angle of $\theta_{max}=53.1^\circ$ with respect to the cavity normal (see Supplementary Figure S1). For the device discussed in the main manuscript (see Figs.3,4), having an on-axis ($\theta=0$) resonance wavelength of 925nm, the shortest wavelength that can be collected is hence 556nm. The measured microcavity-controlled emission spectra typically level off at around 850nm and have a spectral width of 40nm (FWHM), which translates into an angular distribution of $\theta=12^\circ$ (FWHM), with an intensity maximum occurring at $\theta_{max}=5^\circ$ (see Supplementary Figure S1). This demonstrates that the cavity-coupled thermal emission of graphene is radiated into a narrow lobe and that off-axis emissions coupled to guided modes are insignificant.

Estimating temperature effects in a microcavity-controlled graphene transistor

At high source-drain bias, the saturation current density j_{sat} in graphene depends on the self-heating of the graphene layer²². The degree of self-heating is determined by the thermal coupling of graphene to its environment. A measure for the thermal coupling is the thermal conductance r . Within the self-heating model the saturation current is proportional to the square root of the thermal conductance,

$$j_{sat} \propto r^{0.5}$$

We extract a lower bound for the thermal conductance r_0 in our graphene transistors by fitting in Supplementary Figure S2 the measured spectra of the free space, non-confined thermal radiation to the following expression

$$T = T_{amb} + j \cdot F/r_0$$

which delivers $r_0=0.4 \text{ kW}/(\text{cm}^2\text{K})$.

We now estimate the temperature modifications ΔT associated with the optical confinement based on the expression

$$\Delta T = \frac{j_{sat} F}{r}$$

We assume that $j_{sat}=j \cdot j_{sat,0}$ for $j > j_{sat,0}$ and that relative changes in the thermal conductance r can be captured through the relative changes of the saturation current

$$r = r_0 \left(\frac{j_{sat}}{j_{sat,0}} \right)^2$$

As reference saturation current $j_{sat,0}$, we choose the current density at the intersection between regimes I. and II. (see Supplementary Figure S4).

The resulting temperature modifications for the cavity emitter discussed in Figs. 3, 4 of the main manuscript are plotted in Supplementary Figure S4. As compared to graphene in free, non-confined space, the modifications of saturation current suggest temperature modifications as high as $\Delta T=100\text{K}$.

Supplementary References

- 28 Becker, H., Burns, S., Tessler, N. & Friend, R. Role of optical properties of metallic mirrors in microcavity structures. *J Appl Phys* **81**, 2825–2829 (1997).